arXiv:1406.4913v1 [astro-ph.EP] 18 Jun 2014

The Opposition Effect of the Asteroid 4 Vesta

Sunao Hasegawa,[1] Seidai Miyasaka,[2] Noritaka Tokimasa,[3] Akito Sogame,[4] Mansur A. Ibrahimov,[5] Fumi Yoshida,[6] Shinobu Ozaki,[7] Masanao Abe,[1] Masateru Ishiguro,[8] and Daisuke Kuroda[9]

[1]*Institute of Space and Astronautical Science, Japan Aerospace Exploration Agency, 3-1-1 Yoshinodai, Chuo-ku, Sagamihara, Kanagawa 252-5210, Japan*
hasehase@isas.jaxa.jp

[2]*Tokyo Metropolitan Government, 2-8-1 Nishishinjyuku, Shinjyuku, Tokyo 163-8001, Japan*

[3]*Sayo Town Office, 2611-1 Sayo, Sayo-cho, Sayo, Hyogo 679-5380, Japan*

[4]*School of Engineering, Tokai University, 4-1-1 Kitakaname, Hiratsuka, Kanagawa 259-1292, Japan*

[5]*Space Astrometry Department, Institute of Astronomy of the Russian Academy of Sciences, 48 Pyatnitskaya Street 119017, Moscow, Russia*

[6]*Office of International Relations, National Astronomical Observatory of Japan, 2-21-1 Osawa, Mitaka, Tokyo 181-8588, Japan*

[7]*TMT Project Office, National Astronomical Observatory of Japan, 2-21-1 Osawa, Mitaka, Tokyo 181-8588, Japan*

[8]*Department of Physical and Astronomy, Seoul National University, 1 Gwanak-ro, Gwanak-gu, Seoul 151-742, Korea*

[9]*Okayama Astrophysical Observatory, National Astronomical Observatory of Japan, 3037-5 Honjo, Kamogata-cho, Asakuchi, Okayama 719-0232, Japan*

(Received ; accepted)

Abstract

We present the results of photometric observations carried out with four small telescopes of the asteroid 4 Vesta in the B, $R_{\rm C}$, and z' bands at a minimum phase angle of 0.1°. The magnitudes, reduced to unit distance and zero phase angle, were $M_B(1,1,0) = 3.83 \pm 0.01, M_{R_{\rm C}}(1,1,0) = 2.67 \pm 0.01$, and $M_{z'}(1,1,0) = 3.03 \pm 0.01$ mag. The absolute magnitude obtained from the IAU H–G function is ∼0.1 mag darker than the magnitude at a phase angle of 0° determined from the Shevchenko function and Hapke models with the coherent backscattering effect term. Our photometric measurements allowed us to derive geometric albedos of 0.35 in the B band, 0.41 in the $R_{\rm C}$ band, and 0.31 in the z' bands by using the Hapke model with the coherent backscattering effect term. Using the Hapke model, the porosity of the optically active regolith on Vesta was estimated to be $\rho = 0.4$–0.7, yielding the bluk density of 0.9–2.0 $\times 10^3$ kg m^{-3}. It is evident that the opposition effect for Vesta makes a contribution to not only the shadow-hiding effect, but also the coherent backscattering effect that

appears from ca. 1°. The amplitude of the coherent backscatter opposition effect for Vesta increases with a brightening of reflectance. By comparison with other solar system bodies, we suggest that multiple-scattering on an optically active scale may contribute to the amplitude of the coherent backscatter opposition effect (B_{C0}).

Key words: Planetary Systems — minor planets, asteroids: individual (Vesta) — minor planets, asteroids: general — techniques:photometric

1. Introduction

The asteroid 4 Vesta was the last of four asteroids first discovered by H.W. Olbers in 1807. Vesta is the brightest of the main-belt asteroids observed from Earth, and has been the subject of numerous observational studies.

The diameter of Vesta was determined in the 1820s (Aspin 1825) using a micrometrical measure. The albedo value and brightness variation of Vesta were also both measured prior to 1990 (Harrington 1883). Bobrovnikoff (1929) first determined the rotational periods and spectrum of Vesta. Evaluation of the perturbations due to Vesta during an asteroid approach near Vesta allowed derivation of the mass of Vesta (Hertz 1968). A radiometric technique was first applied to determine an accurate albedo and diameter for an asteroid (Vesta) by Allen (1970). McCord, Adams, & Johnson (1970) showed that certain basaltic achondrite meteorites can be linked by visible reflectance measurements to Vesta. Using lightcurves for Vesta, two possible solutions of pole orientation and the existence of a south pole crater were proposed (Taylor 1973). Larson & Fink (1975) concluded, based on spectroscopic data obtained at near-infrared wavelengths, that the Vestan surface is covered with eucrites, which are part of the howardite–eucrite–diogenite (HED) achondrite meteorite clan. Disk resolved images of Vesta have been derived from speckle interferometry techniques (Worden et al. 1977). Degewij, Tedesco, & Zellner (1979) monitored Vesta polarimetrically and concluded that it has a nearly spheroidal shape with a heterogeneous surface. Ultraviolet spectra were obtained for Vesta using the International Ultraviolet Explorer (IUE: Boggess et al. 1978), and the results supported the link between Vesta and HED meteorites (Butterworth et al. 1980). Drummond, Eckart, & Hege (1988) delineated surface patterns on Vesta from speckle interferometric observations. Centimeter and millimeter observations indicate the presence of dusty regolith on the surface of Vesta (Johnston et al. 1989). From radar albedo and the circular polarization ratio obtained using radar observations, Vesta has been shown to have a basaltic and immature regolith surface (Mitchell et al. 1996). Disk resolved images with the Hubble Space Telescope (HST) allowed surface color variations and topographic features of Vesta to be mapped in detail (Thomas et al. 1997). Müller & Lagerros (1998) conducted a thermal inertia study of the surface of Vesta using a combination of thermal radiation data from the Infrared Astronomical Satellite (IRAS: Neugebauer et al. 1984), Infrared Space Observatory (ISO: Kessler et al. 1996), and

ground-based observatories. Dotto et al. (2000) and Heras et al. (2000) noted that olivine-associated spectral features are evident on the surface of Vesta using an ISO Photo-Polarimeter and Short Wavelength Spectrometer, respectively. The detection of a hydrated absorption feature in Earth-based KL band measurements has been interpreted to represent carbonaceous chondritic ejecta and space weathering on Vesta (Hasegawa et al. 2003). Prior to the Dawn spacecraft's rendezvous with Vesta (Russell et al. 2012), remote sensing measurements using ground- and space-based observatories had revealed many aspects of the physical properties of Vesta, as described above.

The opposition effect is the brightening of a particulate medium back in the direction toward a light source, and is also known as the non-linear surge at small phase angles. The opposition effect was first observed for Saturnian rings by Seeliger (1895), for the Moon by Barabashev (1922), for Mars by O'Leary (1967), and for Iapetus by Franklin & Cook (1974). The opposition effect from an asteroid was recognized for the first time by Gehrels (1956). Gehrels & Taylor (1977) compared the opposition effects of five asteroids. Compiling previous data at phase angles of less than 0.3°, Belskaya & Shevchenko (2000) studied the opposition effect for 33 asteroids comprising various spectral types. Characteristics of the opposition effect of 21 dark asteroids were obtained down to phase angles of 0.1°–0.9° (Shevchenko et al. 1997, 2002, 2008, 2012).

The shadow-hiding and coherent backscattering enhancement mechanisms are considered to be major contributors to the opposition effect. For high-albedo objects, such as E-type asteroids (Harris et al. 1989) with a mean geometric albedo of 0.55 ± 0.21 (Usui et al. 2013, 2014) and Galilean satellites (Thompson & Lockwood 1992) with a high albedo of ∼0.8 (Buratti 1995), the point where the brightness changes from linear growth to a steeply sloped surge is in the range of several degrees. The opposition effect for higher-albedo surfaces is generally explained by coherent backscattering enhancement (Muinonen et al. 2002, Dlugach & Mishchenko 2013). Kaydash et al. (2013) proposed that coherent backscattering enhancement partially contributes to the opposition effect of the Moon, which has a medium albedo that is lower than that of Vesta at phase angles less than 2°. Some dark asteroids display a large opposition effect over a range of phase angles less than 1° (Belskaya et al. 2002). Therefore, observations at low phase angles (i.e., less than 1°) are important to constrain the properties of the opposition effect for asteroids.

The opposition effect for Vesta was first detected by Gehrels (1967). Photometric observations of Vesta, including at small phase angles less than several degrees, have been carried out in numerous studies (1.9°; Gehrels 1967, 2.5°; Taylor 1973, 1.4°; Lagerkvist et al. 1989, 1.7°; Lagerkvist & Magnusson 1990, 1.3°; Rock & Hollis 1990, 1.2°; Lagerkvist et al. 1992). The Dawn spacecraft obtained photometric images whilst orbiting 4 Vesta at phase angles from 7.7° to 107.5° (Li et al. 2013). However, photometric data for Vesta at less than 1°, which would allow a robust investigation of the opposition effect, have not yet been

obtained.

On January 5 2006, the phase angle of Vesta was located at 0.1°, and such a small phase angle (less than 1.0°) will not happen again until 2029. To investigate the characteristics of the opposition effect and phase function at an extremely low phase angle for 4 Vesta, we obtained photometric data for Vesta from December 2005 to April 2006. Here we present these photometric observations. This paper describes the observations and data reduction procedures (Section 2), acquisition of the photometric data (Section 3), phase function results (Section 4), and a discussion of these results (Section 5).

2. Observations and data reduction procedures

The observations of Vesta were performed using six different telescopes at five locations in Japan and Uzbekistan, including photometry between December 2005 and April 2006, and spectroscopy during February and March 2006, and January 2014. Photometric data were obtained at the Institute of Space and Astronautical Science (ISAS), Japan Aerospace Exploration Agency (JAXA) in Kanagawa, Japan (no MPC code; 139°23'43"E, 35°33'29"N; 140 m), Miyasaka Observatory in Yamanashi, Japan (MPC code 366; 138°17'50"E, 35°51'57"N; 860 m), Nishiharima Astronomical Observatory in Hyogo, Japan (no MPC code; 134°20'09"E, 35°01'33"N; 450 m), and Maidanak Astronomical Observatory in Qashqadaryo, Uzbekistan (no MPC code; 66°53'51"E, 38°40'25"N; 2600 m). Spectroscopic data were recorded at the Nishiharima Astronomical Observatory and the Okayama Astrophysical Observatory, National Astronomical Observatory of Japan in Okayama, Japan (MPC code 371; 133°35'38"E, 34°34'37"N; 360 m).

2.1. Photometric observations

Photometric observations of Vesta were recorded for 30 nights. The nightly observing details are summarized in Table 1.

Eighteen nights of photometric observations were made with a refracting telescope with an aperture of 0.064 m and a focal ratio of 2.8 at ISAS, JAXA, in Sagamihara. This telescope was installed temporarily for this study on the roof of the research/administration building. An SBIG ST-10XME with a Kodak KAF-3200ME detector yielded a format of 2184 × 1472 pixels with an image scale of $7\farcs8$/pixel and a sky field of $282\farcm6 \times 190\farcm8$. The full-width half maximum of stellar images at this site was typically 3–5″. The resolution is smaller than the pixel size, but star images were spread out over several pixels due to the imaging performance of the telescope and CCD. Johnson B, Cousins $R_{\rm C}$, and Sloan Digital Sky Survey (SDSS) z' filters were used for these observations. Flat fielding observations were performed using the 0.6 m integrating sphere constructed in the same way as described by Sogame et al. (2005).

Fifteen nights of photometric observations were obtained using the Ritchey–Chrétien

[1] ⟨http://ssd.jpl.nasa.gov/horizons.cgi#top⟩.

telescope with an aperture of 0.36 m and a focal ratio of 8.0 at the Miyasaka Observatory. This telescope was equipped with an SBIG STL-1001E CCD camera with a Kodak KAF-1001E detector whose format is 1024 × 1024 pixels. This system produced image dimensions of 1.″7/pixel, yielding a field of view of 29.′4 × 29.′4. The typical full-width half maximum of stellar images at this site was 3–5″. Johnson B, Cousins $R_{\rm C}$, and SDSS z' filters were used for the observations. Dome flat fielding images were obtained from this 0.36 m telescope.

Seven nights of photometric observations were conducted using a refracting telescope with an aperture of 0.076 m and a focal ratio of 8.0 at the Nishiharima Astronomical Observatory. This telescope is usually equipped with a 0.60 m reflecting telescope as a guide scope. The data were recorded with an SBIG ST-9 CCD camera and Kodak KAF-0261 detector (512 × 512 pixels; angular resolution of 6.″9/pixel); sky field of 58.′8 × 58.′8). The full-width half maximum of stellar images at this site was typically 1–3″. The resolution is less than a pixel size, but star images spread out over several pixels due to the imaging performance of the telescope and CCD. This telescope was equipped with Johnson B, Cousins $R_{\rm C}$, and SDSS z' filters. Measurements of flat fielding were made through the 0.6 m integrating sphere, which are similar to those made at the Sagamihara site.

A single night of photometric observation was recorded using a Zeiss reflecting telescope with an aperture of 0.60 m and a focal ratio of 12.5 at the Maidanak Astronomical Observatory. This telescope is equipped with a FLI 1000IMG CCD camera with a IMG1001E Kodak chip, which yielded an image format of 1024 × 1024 pixels and the projected area was 11.′7 × 11.′7, corresponding to an angular resolution of 0.″7/pixel. The typical full-width half maximum of stellar images at this site was ca. 1″. Johnson B and Cousins $R_{\rm C}$ filters were used for these observations. Flat fielding images were taken during the evening and/or morning twilight using this 0.60 m telescope.

HD 268518 was selected for calibration in this study because of its close proximity to Vesta from 28 December 2005 to 8 January 2006, and because of its G0 spectral classification, which suggests that this star is a solar analog. HD 268518 ($B = 8.193$ and $R_{\rm C} = 7.227$ mag) is a standard star in the Johnson–Cousins photometric system, which is based on the Vega magnitude system (Oja 1996). Since HD 268518 is not a standard star in the SDSS photometric system, which is based on the AB magnitude system, it was calibrated with respect to the SDSS standard stars SA 97 249, SA 97 284, SA 97 288, SA 97 345, SA 97 351, SA 100 280, and SA 100 394 (Smith et al. 2002), resulting in $z' = 7.260$ mag. The accuracy of the absolute photometry is estimated to be 0.01–0.04 mag.

All photometry was performed differentially relative to on-chip comparison stars, and then scaled to match the calibrated data. In this study, integrations of the standard star and all comparison stars without variable stars were rapidly alternated as both fields overlapped through the same airmass using the 0.064 m telescope with a very large field of view. This observation method, which is made differentially with respect to nearby calibrated comparison

stars, is considerably more efficient and accurate than only using catalog standards (Harris et al. 1989). This approach also minimizes the effects of atmospheric extinction and weather changes. The observational data, except for those obtained at the Sagamihara site, were calibrated by selecting comparison stars from the standard comparison stars, which were scaled to the photometric levels of HD 268518 as observed at the Sagamihara site.

Sidereal tracking was used for all photometric observations. Since the integration times were short, the non-sidereal movement of Vesta during the integrations was smaller than the seeing size. The dark images for correction were constructed from a median combination of 10–20 dark frames. Stacked flat fielding images for correction were created by a median combination of 10–20 flat fielding frames. All photometric image frames for an individual night were bias-subtracted and flat-fielded using Image Reduction and Analysis Facility (IRAF) software. The fluxes of the asteroids and comparison stars were measured through circular apertures with a diameter of more than four times that of the full-width at half maximum size, using the APPOT task in IRAF.

The observed magnitude, $m_\lambda(1,\,1,\,\alpha)$, which is defined at a location of 1 AU from both the Sun and the Earth, and at a phase angle α° in a given filter, is calculated using the following equation:

$$m_\lambda(1,1,\alpha) = m_\lambda(R_\mathrm{h},\Delta,\alpha) - 5\log(R_\mathrm{h}\Delta), \tag{1}$$

where $m_\lambda(R_\mathrm{h},\Delta,\alpha)$ is the observed apparent magnitude in the observed filter, R_h is the heliocentric distance, Δ is the geocentric distance, and α is the phase angle of Vesta.

2.2. Spectroscopic observations

The spectroscopic observations were carried out at the Nishiharima Astronomical Observatory in Japan using the Nayuta 2.0 m telescope with an optical spectrograph and E2V CCD 42-40, yielding images of 2048 × 2048 pixels (Hasegawa et al. 2006). The spectrograph, the Medium And Low-dispersion Long-slit Spectrograph (MALLS), was attached to the f/12 Nasmyth focus of the Nayuta telescope. A 150 line/mm grating with a dispersion of 338 Å/mm in the first order was used. The back-illuminated CCD has square 13.5 μm pixels, giving a dispersion of ca. 2.5 Å/pixels in the wavelength direction. The slit length is 5′.0 in the cross-wavelength direction and the covered spectral range is ca. 0.49–0.98 μm.

The spectroscopic data were taken by the Kyoto Okayama Optical Low dispersion Spectrograph (KOOLS) (Ohtani et al. 1998, Ishigaki et al. 2004) attached to the f/18 Nasmyth focus of the Okayama Astrophysical Observatory's 1.88 m telescope. A grism with a 6563 Å/mm blaze was used. The SITe ST-002A CCD has square 15.0 μm pixels, giving a dispersion of ca. 3.8 Å/pixels in the wavelength direction. The slit length is 4′.4 in the cross-wavelength direction and the covered spectral range is ca. 0.49–0.94 μm.

Particular care was taken on the choice of the slit width, in order to mitigate the con-

sequences of atmospheric differential refraction (Filippenko 1982). This is an important problem in asteroidal photometric spectroscopy. The possible loss of photons at both ends of the spectrum cloud can lead to erroneous classification of the asteroid spectral type and a false calculation of spectral slope. Ideally, the slit should be perpendicular to the horizon, but the direction of the slit was not be able to be controlled due to issues with the instrument rotator at the Nasmyth focus. Therefore, a wide-width 8" and 6" slit and was used for MALLS and KOOLS observations, respectively.

Vesta was observed during three runs on 27 February and 2 March in 2006, and on 28 January 2014. The typical seeing sizes on the three nights were ∼2". The objects were observed near the meridian with an airmass lower than 2.0. Integration times were determined according to the brightness of each object. Although the Nayuta telescope can track solar system objects in non-sidereal tracking mode, the data were obtained in sidereal tracking mode using a manual offset. The objects were located in the center of the slit using a slit-viewer CCD. The Okayama telescope was used to track asteroids with non-sidereal tracking.

Wavelength calibration frames were taken regularly during the night with light from an iron–neon–argon hollow cathode lamp. The production of reflectance spectra from the wavelength-calibrated spectra is achieved through the division of the spectrum of a G2V Sun-like star. To do this, HD 60298 and G63-51 were observed in 2006 and 2014, respectively. Observations of the standard star were coordinated so that the star was observed at an airmass similar to those of the asteroid (i.e., the airmass difference was less than 0.1 in each case). Since the airmass difference was 0.2 for KOOLS observations, the slope of the spectrum was corrected using the extinction curve of the solar analogue. Flat fields were taken with a halogen lamp. Frames of flat fields were obtained each night and averaged to obtain a high signal-to-noise ratio. The observational details for the spectroscopic observations are listed in Table 2.

All data reduction was performed using the software package IRAF. Although no significant change in flat field frames were observed from one night to another, for each night a separate flat field was used. The bias from the over-scan region of the spectral CCD image was subtracted from all spectra. After subtraction of bias, each object frame was divided by a normalized bias to correct the flat fielding flame. The sky background in each object's spectrum was then fitted individually at each wavelength and subtracted. The two-dimensional spectrum was then collapsed to one dimension, given that all the observed targets were point sources. Following this, the dispersion solution for each iron–neon–argon spectrum was determined. Solar analog standard star was used to compute reflectivities for spectra from the target. The solar spectra were treated in the same way as the asteroid spectra. The spectra were binned with a standard 19 boxcars for MALLS observations and 13 boxcars for KOOLS observations, and the spectral resolution was 0.05 μm.

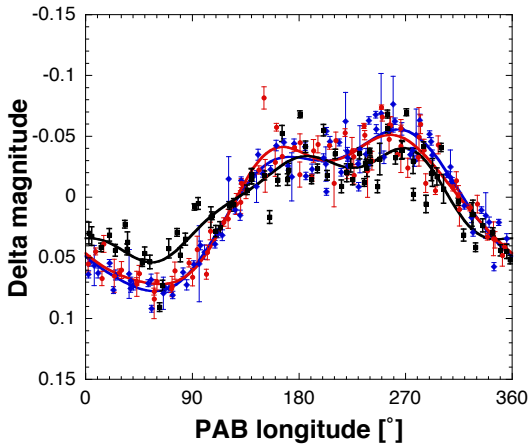

Fig. 1. Composite rotational lightcurve of Vesta. B, R_C, and z' lightcurves of Vesta plotted as a function of the PAB longitude. PAB is the mean of the geocentric and heliocentric positions of the asteroid. The blue diamonds, red circles, and black squares indicate photometric data in the B, R_C, and z' band filters, respectively. The solid line is a fourth-order fit obtained from Fourier analysis.

3. Photometric data

3.1. Lightcurve correction

To obtain the mean magnitudes at the phase angle of 0° for an accurate photometric function, the influence of rotational variation of Vesta must be eliminated. The lightcurve of Vesta is already precisely known (e.g., Stephenson 1951). For the purpose of the rotational variation correction, the lightcurves in the B, R_C, and z' bands were made as a function of the phase angle bisector (PAB) of Vesta longitude. A coordinate system for Vesta has been defined by HST (Thomas et al. 1997). Vesta's PAB longitudes were calculated from the mean values of the apparent planetographic longitude of Vesta and the apparent subsolar planetographic longitude of the Sun. The planetographic longitudes were obtained from the JPL Horizons ephemeris website.[1] Composite lightcurves (plotted in Fig. 1) contain data from multiple rotations with phase angles greater than 9°, where the phase angle changes by less than 0.1° from one rotation to the next, because the change of phase angle is much faster at smaller phase angles.

The line present in all the lightcurves corresponds to a fourth-order Fourier series that best fits each respective data set. The lightcurves in the B, R_C, and z' bands are consistent with previous studies (Reynoldson et al. 1993, Jaumann et al. 1996, Nonaka et al. 2003, Fulvio et al. 2008). Based on these curves as a function of PAB longitude in each band, the corrections for rotational variation were applied to all photometric data obtained by ground-based observations.

3.2. Combining the data with spacecraft observations

It is difficult to observe Vesta from Earth at a phase angle more than ∼25° due to its orbit. The Rosetta spacecraft (Glassmeier et al. 2007) made photometric observations at a phase angle of 52° on the way to comet 67P/Churyumov–Gerasimenko on May 1 2010 (Fornasier et al. 2011). Between May 3 2011 and August 11 2012, Dawn also obtained photometric data at phase angles from 8° to 108° (Li et al. 2013). These data from the Rosetta and Dawn spacecrafts are not able to be obtained from ground-based observations and, therefore, these data were used to supplement the photometric data from this study.

The Rosetta spacecraft conducted observations of Vesta using both narrow- and wide-angle cameras in the OSIRIS camera (Keller et al. 2007) with red filters. Absolute photometric values were obtained with an Bessel R filter. These values can be used without correction as the absolute values in the Cousins $R_{\rm C}$ band. Spectrophotometric data covering the wavelength range 0.27–0.99 μm were also taken by the OSIRIS camera at a phase angle of 52°. The photometric values in the B and z' bands were estimated in combination with the $R_{\rm C}$ band photometric data, solar color, and reflectance data. $(B - R_{\rm C})_{\odot}$ was taken from Ramírez et al. (2012). Based on the transformation equations between the SDSS and Johnson–Cousins photometric systems (Rodgers et al. 2006) and the solar color from SDSS (Ivezić et al. 2001), $(R_{\rm C} - z')_{\odot}$ was determined. The B and z' band reflectances for Vesta were acquired by interpolating spectrophotometric data from Rosetta (Fornasier et al. 2011).

The Dawn spacecraft collected data for a disk-integrated phase function in visible wavelengths with a Framing Camera (Schröder et al. 2013) through a clear filter. The effective wavelength of the clear filter is 0.732 μm, which is similar to the $R_{\rm C}$ band. Given that the filter band of photometric values in Li et al. (2013) reported the Johnson V band, the data were converted through the V band to the $R_{\rm C}$ band using the solar color $(V - R_{\rm C})_{\odot}$ and spectrum of Vesta.

Fig. 2 shows the spectra of Vesta acquired with the Nayuta and Okayama telescopes in this study, as compared with previous studies. The combined spectra from this study is in good agreement with previous studies. For adjustment to the $R_{\rm C}$ band, the spectrum of Vesta obtained in this study was used. The solar color is similar to the value reported by Ramírez et al. (2012). Using these values, the conversion to the $R_{\rm C}$ band was carried out.

4. Phase function

The combined B, $R_{\rm C}$, and z' band data from this study, along with those from Fornasier et al. (2011) and Li et al. (2013), were used for the photometric phase function. The values obtained at each phase angle were compiled in steps of 0.1°. To know the properties of the opposition effect and phase function, the data were fitted with three function models (i.e., the IAU H–G phase function model, the Shevchenko function model, and the Hapke model).

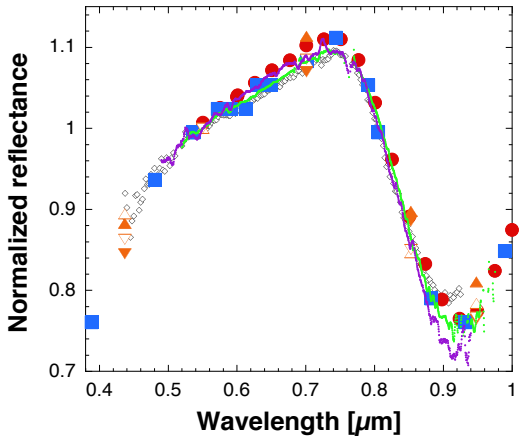

Fig. 2. Comparison of visible spectra for Vesta. Orange triangles, red circles, black diamonds, blue squares, green dots, and purple dots indicate spectra from Zellner, Tholen, & Tedesco (1995), Hicks, Fink, & Grundy (1998), Xu et al. (1995), Bus & Binzel (2002), Fornasier et al. (2011), this study (Nishiharima), and this study (Okayama), respectively. The spectra derived from the Nishiharima and Okayama observations are the combination of four spectra from 2 March 2006 and three spectra from 28 January 2006, respectively. Spectroscopic data for open inverted triangles, open diamonds, open triangles, filled inverted triangles, filled triangles, filled circles, green dots, purple dots, and filled squares are obtained at phase angles of 7.9, 11.9, 15.6, 16.0, 17.5, 19.0, 20.9, 24.9, and 52.5°, respectively.

A routine was employed to obtain a solution that minimizes the χ^2 values for all models, and in which all parameters can be varied to achieve this. The curve fit is based on the Levenberg–Marquardt algorithm, which is commonly employed to solve nonlinear least-squares problems. The χ^2 values are defined as:

$$\chi^2 = \frac{1}{N}\sum_{n=1}^{N}\left[M_\lambda(1,1,\alpha) - m_\lambda(1,1,\alpha)\right]^2, \tag{2}$$

where N is the number of data points, and $M_\lambda(1,1,\alpha)$ is the model magnitude at 1 AU from both the Sun and the Earth and at a phase angle α° in a given filter. Upon χ^2 minimization, the corresponding parameter value was included in the final model set of parameters. The error in the parameter value is the standard error.

4.1. IAU H–G phase function

The IAU H–G phase function model is a simple two-parameter empirical function that was accepted by Commission 20 of the International Astronomical Union (Bowell et al. 1989). This is the most common phase function of asteroids and has the following form:

$$M_\lambda(1,1,\alpha) = H_\lambda - 2.5\log\left[(1-G_\lambda)\Phi_1(\alpha) + G_\lambda\Phi_2(\alpha)\right], \tag{3}$$

where H_λ is the absolute magnitude in the observed band at a phase angle of 0°, and G_λ

is the so-called slope parameter, which describes the shape of the magnitude phase function. $\Phi_1(\alpha)$ and $\Phi_2(\alpha)$ are two basis functions normalized at unity for $\alpha = 0°$. These functions are accurately approximated by:

$$\begin{aligned}\Phi_1(\alpha) &= \exp\left(-3.33\tan^{0.63}\frac{\alpha}{2}\right),\\ \Phi_2(\alpha) &= \exp\left(-1.87\tan^{1.22}\frac{\alpha}{2}\right).\end{aligned} \tag{4}$$

Table 3 lists the H_λ and G_λ values obtained for Vesta in this and previous studies. H_{R_C} and G_{R_C} were fitted by changing the adaptation range of the phase angle to determine a phase angle range consistent with the IAU H–G phase function (see sans-serif fonts in Table 3). Taking a phase angle range provided from the Earth into consideration, H_{R_C} and G_{R_C} decrease whilst the adopted minimum phase angle decreases due to the opposition effect. If the minimum phase angle is more than 7°, which is the onset point of the opposition effect of asteroids (Scaltriti & Zappalà 1980), then the obtained solution is scattered and lost. H_{R_C} and G_{R_C} do not change with an increase in the adopted largest angle until 81.3° due to the linear nature of the magnitude diminution. When the largest phase angle is found at more than 81.3°, the values cannot be correct. Therefore, the appropriate phase angle range for determination of H_{R_C} and G_{R_c} is 0.1–81.3° (see bold fonts in Table 3).

The H_λ and G_λ values that most closely fit the data give $H_B = 3.96 \pm 0.01$, $G_B = 0.30 \pm 0.02$, $H_{R_C} = 2.82 \pm 0.01$, $G_{R_C} = 0.29 \pm 0.01$, $H_{z'} = 3.08 \pm 0.02$, and $G_{z'} = 0.25 \pm 0.01$ mag. The phase curves for Vesta in the B, R_C, and z' bands using the IAU H–G phase function are shown in Fig. 3. The values from the B, R_C, and z' bands from this study are consistent with those of Fornasier et al. (2011) and Reddy et al. (2012). Although the wavelengths used differ, G_λ values from this study are similar to those of previous studies (Minor Planet Circ. 17256, Lagerkvist & Magnusson 1990, Piironen et al. 1997, Velichko et al. 2008, Li et al. 2013).

4.2. Shevchenko function

The Shevchenko phase function model is a simple three-parameter empirical function that was proposed by Shevchenko (1996). This function is a direct definition of the amplitude of the opposition effect and has the following form:

$$M_\lambda(1,1,\alpha) = C_\lambda - \frac{a_\lambda}{1+\alpha} + b_\lambda\alpha, \tag{5}$$

where a_λ is a parameter to characterize the opposition effect amplitude and b_λ is the parameter describing the linear part of the magnitude phase dependence. C_λ is a constant defined by $C_\lambda = m_\lambda(1, 1, 0) + a_\lambda$.

To determine the phase angle range for the Shevchenko phase function, the parameters a_{R_C} and b_{R_C} were fitted by changing the adaptation range of the phase angle. The precision

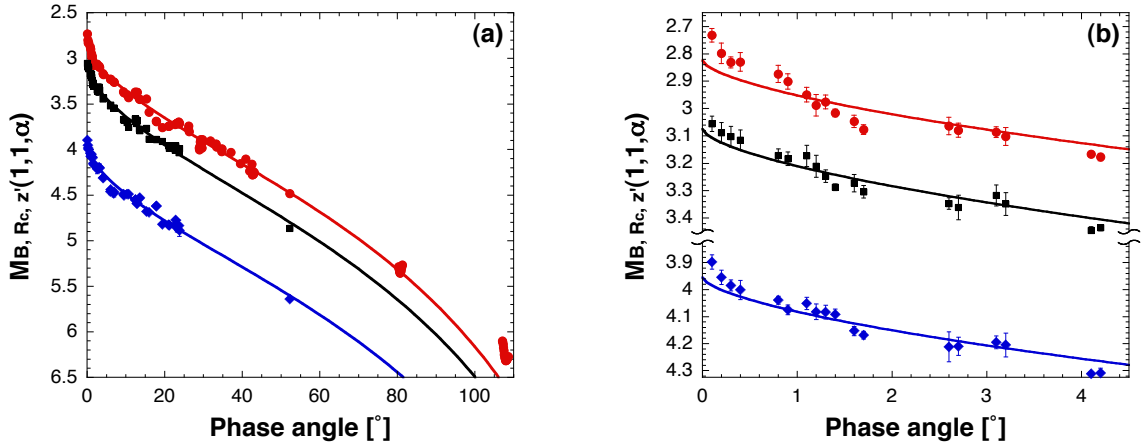

Fig. 3. Fitted phase curves for Vesta using the IAU H–G phase function. (a) and (b) show the whole curves and expanded views at small phase angles, respectively. The blue diamonds, red circles, and black squares are photometric data from the B, $R_{\rm C}$, and z' band filters, respectively. The lines show the best-fit phase curves obtained with the IAU H–G phase function.

of $a_{R_{\rm C}}$ increases when the angle is reduced. When the minimum phase angle is more than 7°, the obtained $a_{R_{\rm C}}$ cannot be correct. This behavior is the same as when fitting results with the IAU H–G phase function (Section 4.1). The parameter $b_{R_{\rm C}}$ is changed until 81.3°, and such that the linear fit degrades. Therefore, the phase angle range for assignment of the parameters in the $R_{\rm C}$ band is changed from 0.1° to 81.3°. The parameters a_λ and b_λ obtained for Vesta in this study are listed in Table 4.

The $M_\lambda(1, 1, 0)$ value for Vesta that fits the data most closely based on the Shevchenko function yields $M_B(1, 1, 0) = 3.85 \pm 0.01$, $M_{R_{\rm C}}(1, 1, 0) = 2.71 \pm 0.01$, and $M_{z'}(1, 1, 0) = 2.98 \pm 0.01$ mag. The phase curves for Vesta in the B, $R_{\rm C}$, and z' bands using the Shevchenko function are shown in Fig. 4.

4.3. Hapke model

The Hapke model is a five-parameter, quasi-experimental function (Hapke 1981, 1984, 1986). This model is based on a physical description of the scattering behavior of a particulate surface and is, therefore, more easily interpretable than empirical models, such as the IAU H–G phase and Shevchenko functions. Still, it is difficult to characterize the physical interpretations based on parameters of the Hapke model. There is no strong correlation between Hapke parameters and the actual physical particle properties (Shepard & Helfenstein 2007, 2011). Hapke (2002) revised this model to incorporate an opposition surge element that takes into account coherent backscatter, and also included an additional term for multiple scattering. However, this model is typically not used unless the phase angle is low (less than 2°). Given that our photometric observations include low phase angles up to 0.1°, the updated Hapke mode (a

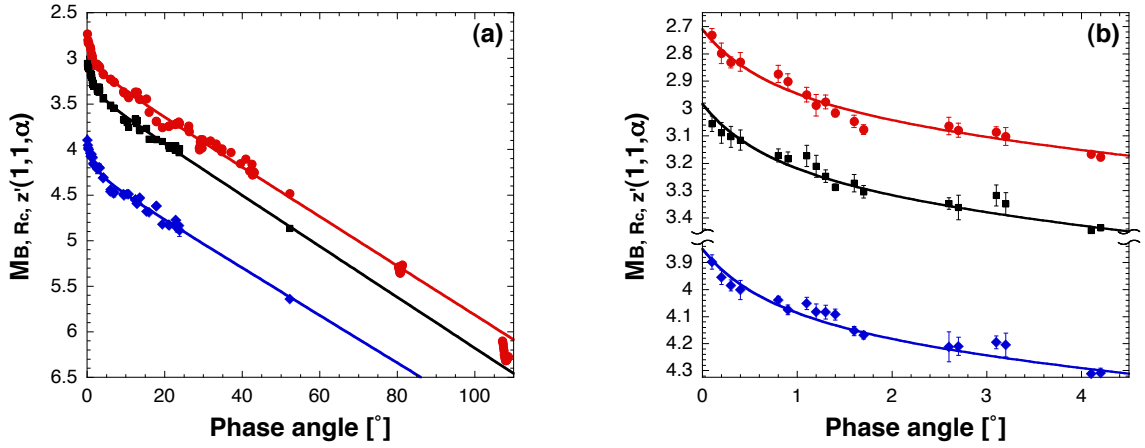

Fig. 4. Fitted phase curves for Vesta using the Shevchenko function. (a) and (b) show whole curves and expanded views at small phase angles, respectively. The blue diamonds, red circles, and black squares are photometric data in the B, $R_{\rm C}$, and z' band filters, respectively. The lines show the best-fit phase curves obtained with the Shevchenko function.

seven-parameter function), as well as the nominal Hapke model, was used in this study.

Hapke (2008) developed the model to express a porosity dependence. However, the updated Hapke model (Hapke 2008) was not used in this study for two reasons, explained below. First, Li et al. (2013) attempted to fit their data using the Hapke model with the relevant porosity parameter (Hapke 2008), but they could not obtain any meaningful results for the porosity parameter. Data for this study contain disk-integrated photometric measurements including small phase angles (less than 1°), but we do not have access to large quantities of disk-resolved photometric data such as Li et al. (2013). It can be predicted easily that the new Hapke model will not yield any meaningful porosity parameter using data from this study. Second, it is hard to obtain a unique solution when the number of unknowns is increased. By reducing the number of fitting parameters by one (in this case, the porosity parameter), a stable solution can be obtained.

The magnitudes in each band were converted to the logarithmic form of I_λ/F_λ (where πF_λ is the incident solar flux and I_λ is the light scattered from the surface).

I_λ/F_λ is expressed as follows:

$$-\frac{5}{2}\log\left(\frac{I_\lambda}{F_\lambda}\right) = M_\lambda(1,1,\alpha) - M_{\lambda\odot} - \frac{5}{2}\log\left(\frac{\pi}{A_{rea}}\right) + M_c, \tag{6}$$

where $M_{\lambda\odot}$ is the magnitude of the Sun at 1 AU in the observed filter (the B-band absolute magnitude is taken from Allen 1976, the $R_{\rm C}$ and z'-band absolute magnitudes are obtained from a combination with $M_{B\odot}$ and the solar colors; Ramírez et al. 2012, Rodgers et al. 2006, Ivezić et al. 2001), A_{rea} is the geometrical cross-section of Vesta in m^2 (Russell et al.

2012), and $M_c = -5\log(1.4960 \times 10^{11}[m]) = -55.87$ is a constant. Given that Vesta is almost spherical (Russell et al. 2012), we used the Hapke model using an integral phase function for a spherical body with a rough surface. The Hapke equation for a spherical body with a rough surface (Hapke 1984, 1986) is given by:

$$\frac{I_\lambda}{F_\lambda} = \left[\left(\frac{w_\lambda}{8}\left[\left(1 + B_{SH_\lambda}(\alpha)\right) P_\lambda(\alpha) - 1\right] + \frac{r_{0_\lambda}}{2}(1 - r_{0_\lambda})\right)\left(1 - \sin\frac{\alpha}{2}\tan\frac{\alpha}{2}\ln\left[\cot\frac{\alpha}{4}\right]\right) + \frac{2}{3}{r_{0_\lambda}}^2\left(\frac{\sin\alpha + (\pi - \alpha)\cos\alpha}{\pi}\right)\right]\left(1 + B_{CB_\lambda}(\alpha)\right) K_\lambda(\alpha, \bar{\theta}_\lambda), \quad (7)$$

where w_λ is the single-particle scattering albedo in a particular band. The term r_{0_λ} is given by:

$$r_{0_\lambda} = \frac{1 - \sqrt{1 - w_\lambda}}{1 + \sqrt{1 - w_\lambda}}, \quad (8)$$

The one-term Henyey–Greenstein single-particle phase function solution (Henyey & Greenstein 1941) is:

$$P_\lambda(\alpha) = \frac{(1 - {g_\lambda}^2)}{(1 + 2g_\lambda\cos(\alpha) + {g_\lambda}^2)^{3/2}}, \quad (9)$$

where g_λ is an asymmetry factor. $K_\lambda(\alpha, \bar{\theta}_\lambda)$ corrects the surface roughness with the surface roughness parameter $\bar{\theta}_\lambda$ (Hapke 1984). The opposition effect term of the shadow-hiding $(B_{SH_\lambda}(\alpha))$ is given by:

$$B_{SH_\lambda}(\alpha) = \frac{B_{S0_\lambda}}{1 + \frac{1}{h_{S_\lambda}}\tan\frac{\alpha}{2}}, \quad (10)$$

where B_{S0_λ} describes the amplitude of the shadow-hiding opposition effect and h_{S_λ} is the width of the shadow-hiding opposition effect peak in radian. The coherent backscatter opposition effect $(B_{CB_\lambda}(\alpha))$ (Hapke 2002) is given by:

$$B_{CB_\lambda}(\alpha) = B_{C0_\lambda}\frac{1 + \frac{1 - \exp\left(-\frac{1}{h_{c_\lambda}}\tan\frac{\alpha}{2}\right)}{\frac{1}{h_{c_\lambda}}\tan\frac{\alpha}{2}}}{2\left(1 + \frac{1}{h_{c_\lambda}}\tan\frac{\alpha}{2}\right)^2}, \quad (11)$$

where B_{C0_λ} describes the amplitude of the coherent backscatter opposition effect and h_{C_λ} is the width of the coherent backscatter opposition effect peak in radian.

Parameters in the Hapke model are constrained by the strength and shape of the phase curves: w_λ is determined by the absolute values of the phase curves; g_λ is controlled by the shape of the curves at all phase angles; $\bar{\theta}_\lambda$ is affected by the shape of the phase function at large phase angles; B_{S0_λ} and h_{S_λ} are obtained from the shape and the intensity of the phase curve

in the phase angle range between 0 and 20°; and B_{C0_λ} and h_{C_λ} are provided by the intensity of the spike phase curve in a phase angle range within several degrees.

Photometric data in R_C were covered over a phase angle from 0.1° to 108.6°, but those in the B and z' bands were obtained from 0.1° and 52.3°. Helfenstein & Veverka (1989) indicated that $\bar{\theta}$ affected the phase function at phase angles greater than 40°. Data in the B and z' bands at phase angles in excess of 40° are indispensable to constrain $\bar{\theta}_B$ and $\bar{\theta}_{z'}$. Li et al. (2013) showed that $\bar{\theta}$ in the visible wavelength range from 0.44 to 0.96 μm, in both cases, is concentrated within a small range of ± 2° at ca. 18°. This study also identified any wavelength independence with respect to $\bar{\theta}$. To reduce the parametric fit to the model, the $\bar{\theta}_\lambda$ value of Li et al. (2013) was adopted in our study.

The phase angle range in the R_C band for the IAU H–G and Shevchenko functions was adopted from 0.1° to 81.3° (see Sections 4.1 and 4.2). For the Hapke model, the phase angle ranged between 0.1° and 81.3°.

The geometric albedo (A_{p_λ}) is defined as the fraction of incident light scattered by the surface at a phase angle 0° relative to a similar sized Lambert disk based on the same observing geometry. The bond albedo (A_{B_λ}) is defined as the total radiation reflected from an object as compared with the total incident radiation from the Sun, which is given by $A_{B_\lambda} = q_\lambda \; A_{p_\lambda}$, where q_λ is the value of the phase integral defined as:

$$q_\lambda = 2 \int_0^\pi \frac{\phi_\lambda(\alpha)}{\phi_\lambda(0)} \; \sin(\alpha) \; d\alpha. \tag{12}$$

where $\phi_\lambda(\alpha)$ is defined in Eq. 6 as I_λ / F_λ.

Two independent determinations of the Hapke parameters were performed with and without inclusion of coherent backscatter opposition effect terms. The Hapke parameters for Vesta, including a comparison with previous studies, are listed in Table 5.

The phase functions for Vesta in the B, R_C, and z' bands using the Hapke model, with or without the coherent backscatter opposition effect terms, are shown in Fig. 5. $M_\lambda(1, 1, 0)$ employing the coherent backscatter opposition effect terms that most closely fit the data gives $M_B(1, 1, 0) = 3.83 \pm 0.01$, $M_{R_C}(1, 1, 0) = 2.67 \pm 0.01$, and $M_{z'}(1, 1, 0) = 3.03 \pm 0.01$ mag. Fig. 6 shows the geometric albedo obtained in this and previous studies. The spectral photometric data in this study, obtained using the coherent backscatter opposition effect terms, are in reasonably good agreement with the spectrum. A visible geometric albedo of 0.342 for Vesta by AKARI (Usui et al. 2011) is consistent with this study without the coherent backscatter opposition effect term. This consistency occurs because the visible photometric data using AKARI did not include small phase angles.

4.4. Error analysis

In general, any standard statistical errors obtained from standard fitting routines including the Levenberg–Marquardt algorithm used in this study, premises that all parameters are

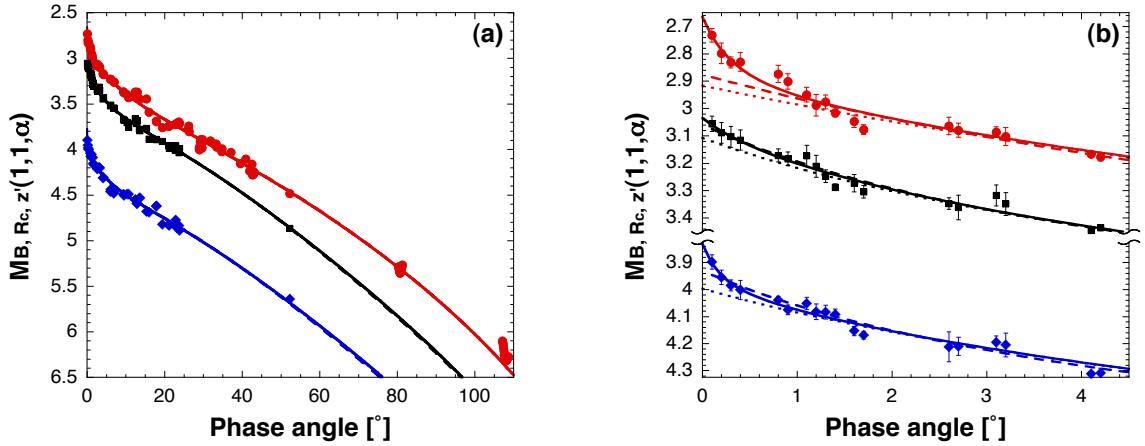

Fig. 5. Fitted phase curves for Vesta obtained with the Hapke model. (a) and (b) show whole curves and expanded views of the curves at small phase angles, respectively. The blue diamonds, red circles, and black squares are photometric data in the B, $R_{\rm C}$, and z' band filters, respectively. The solid, dotted, and dashed lines show the best-fit phase curves obtained with the Hapke model using the coherent backscatter terms, coherent backscatter terms at $B_{C0_\lambda} = 0$, and only shadow-hiding terms, respectively.

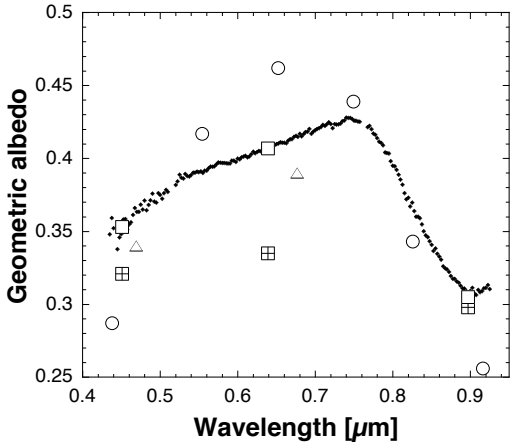

Fig. 6. Comparison of geometric albedo for Vesta. The dots, open triangles, open circles, crossed squares, and open squares represent the geometric albedo from a spectroscopic study (Bus & Binzel 2002), HST (Li et al. 2011), Dawn (Li et al. 2013), and this study without and with coherent backscatter opposition effect terms, respectively. The Vestan spectrum is scaled to match the geometric albedo in the $R_{\rm C}$ band in this study with coherent backscatter opposition effect terms.

independent of each other. However, it is known that each parameter of the Shevchenko function and Hapke models are strongly coupled (e.g., Belskaya & Shevchenko 2000, Helfenstein & Shepard 2011). The standard errors obtained from the algorithm underestimate uncertainties sometimes when applied to fits of the model which has coupled parameters. Helfenstein & Shepard (2011) indicated that standard statistical error estimation techniques can severely underestimate uncertainties in case of the model which has interdependence parameters such as the Hapke model. Therefore, the error for the Shevchenko function and Hapke models in this study may be underestimated.

5. Discussion

The magnitudes at a phase angle of 0° ($M_\lambda(1,\ 1,\ 0)$) obtained with the Shevchenko function and Hapke model, including the coherent backscatter opposition effect terms, are ∼0.1 mag brighter than the absolute magnitude H_λ, which is equal to $M_\lambda(1,\ 1,\ 0)$ obtained using the IAU H–G function (Table 3, 4, and 5). Belskaya & Shevchenko (2000) reported that approximations for various spectral types of asteroids using the H–G function can deviate from the observed magnitude by up to 0.1 mag. This reflects the fact that the H–G function has only two parameters, which are insufficient to properly model the opposition effect.

The Shevchenko function is a simple three-parameter model, which includes a parameter that directly expresses the opposition effect. The distribution of the parameter describing the amplitude of opposition brightening (a) and the coefficient for the linear part of the phase curve (b) obtained by the Shevchenko model as a function of the geometric albedo of asteroids are shown in Fig. 7. Belskaya & Shevchenko (2000) showed that a decreases for both dark and high-albedo asteroids, and that the largest a values characterize moderate-albedo asteroids. These authors also reported that b increases linearly as the logarithm of geometric albedo decreases. The Shevchenko function parameters for Vesta obtained in our study are not inconsistent with this previous study. The correlation of parameters from the Shevchenko function can be expressed by:

$$a = \begin{cases} 0.24 - 0.33\log(p_\lambda), & \text{for} \quad 0.22 < p_\lambda, \\ 0.75 + 0.44\log(p_V), & \text{for} \quad p_\lambda < 0.22, \end{cases} \tag{13}$$

$$b = 0.015 - 0.022\log(p_\lambda), \tag{14}$$

where p_λ is the geometric albedo at the observed filter band. The geometric albedo can be estimated by the Shevchenko parameters in equation 13 and/or 14.

The spectra of Vesta in the wavelength range between the B and z' bands yield several-percent precision for phase angles from 8 to 53° (see Fig. 2). The Vestan colors ($B - R_C$) and ($z' - R_C$) based on the Hapke model including the coherent backscattering effect (Fig. 8) show differences in color within several percent up to 40°. This indicates a weak phase angle

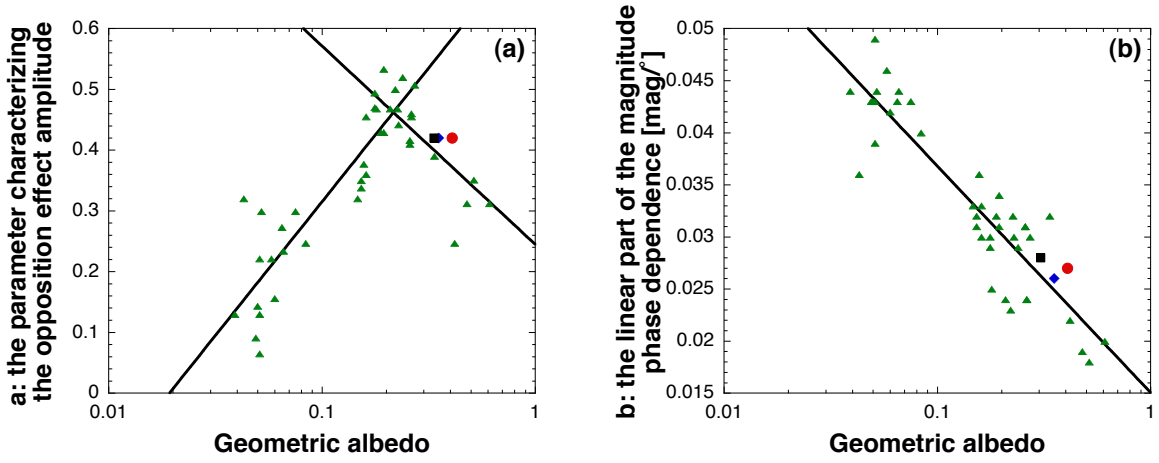
a: the parameter characterizing the opposition effect amplitude
(a)
Geometric albedo
b: the linear part of the magnitude phase dependence [mag/°]
(b)
Geometric albedo

Fig. 7. Relationship between the geometric albedo and parameters of the Shevchenko function. The geometric albedo of Vesta was obtained from the Hapke model. The parameters a and b for asteroids, apart from Vesta, were taken from Belskaya et al. (2002), Shevchenko et al. (2002), and Belskaya et al. (2003). The geometric albedos for other asteroids are from Usui et al. (2011). The blue diamond, red circle, black square, and green triangles are data for Vesta in the B, $R_{\rm C}$, and z' band filters, and asteroids except Vesta, respectively.

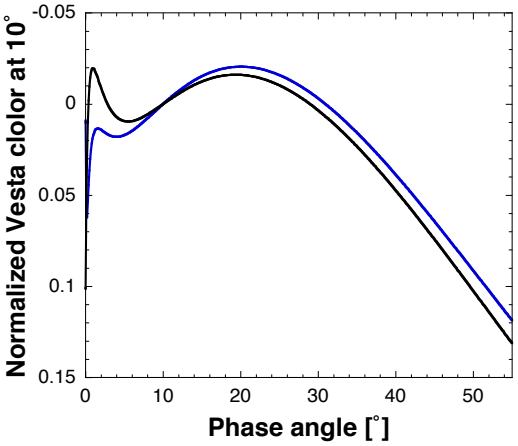

Fig. 8. Vestan color as a function of phase angle using the Hapke model, including the coherent backscattering effect. The blue and black lines indicate $(B - R_{\rm C})$ and $(z' - R_{\rm C})$ for Vesta, respectively. The color was normalized at a phase angle of 10°.

dependence of Vesta's spectrum.

The width of the shadow-hiding opposition effect peak h_{S_λ} of the Hapke model can be interpreted in terms of the porosity and grain size distribution of the optically active regolith (Hapke 1986). h_{S_λ} is given by:

$$h_{S_\lambda} = -\frac{3}{8} Y \ln \rho_\lambda, \tag{15}$$

where Y and ρ_λ describe the grain size distribution and porosity of the particles in an optically active scale, respectively. Various cases are considered for Y (Hapke 1986). Y for the lunar regolith, which is probably similar to the surfaces of many other small bodies (Hapke 1986), has the form:

$$Y = \frac{\sqrt{3}}{\ln\left(\frac{d_l}{d_s}\right)}, \tag{16}$$

where d_l and d_s describe the diameter of the largest and smallest particles of the optically active regolith, respectively.

The particle size of the Apollo soil samples ranges from several millimeters to several microns (Carrier 1973). Therefore, the ratio of d_l and d_s is $\sim 10^3$. Gundlach & Blum (2013) estimated the nature of the regolith of various bodies, including the Moon and Vesta, using remote measurements of the thermal inertia. The calculated diameter of the lunar regolith material is $\sim$100 μm, which is in agreement with the mean value measured on Apollo samples. The regolith grain size of Vesta is similar to that of the Moon. The Dawn spacecraft has observed the surface of Vesta extensively. Its surface is heavily cratered, like that of the Moon (Jaumann et al. 2012, Russell et al. 2012). The regolith of the Moon and Vesta formed as ejecta produced by collisional impacts at their surface (e.g., McKay et al. 1989). Hiroi, Pieters, & Takeda (1994) suggested that significant fine regolith particles (less than 25 μm) are present on the surface of Vesta. These observations all imply that the d_l and d_s of Vesta are similar to those of the Moon. Therefore, the ratio of d_l and d_s for the Moon is used in equation 16 for Vesta. The porosity of Vesta (ρ_B = 0.575–0.7, ρ_{R_C} = 0.4–0.5, $\rho_{z'}$ = 0.65–0.7) is similar to that of the Moon (Helfenstein & Veverka 1987), and less than that of the asteroids 243 Ida and 433 Eros (Domingue et al. 2002), which have lower gravity than both Vesta and the Moon. Most of the surface of Vesta is covered with eucrite-rich howardites and/or cumulate or polymict eucrites (De Sanctis et al. 2013). Howardites and eucrites have a grain density of between 3.0 $\times$ 10^3 and 3.3 $\times$ 10^3 kg m^{-3} (Britt & Consolmagno 2003). The bulk density is derived from (1 $-$ porosity) $\times$ the grain density. The bulk density of Vestan soil in the optically active region is 0.9–2.0 $\times$ 10^3 kg m^{-3}. This is not inconsistent with a previously derived result that Vesta has a fairly loose and fluffy dust layer on its surface, based on passive microwave observations (Redman et al. 1992).

The bulk densities in each filter decrease with the reduction of the geometric albedos. In general, the optical depth of the powder depends on the transparency of the particles. The bulk density of lunar regolith increases with the depth (Houston et al. 1974). Therefore, the density obtained at wavelengths of low reflectance may represent only information from shallower depths.

In this study, the results of the Hapke model with and without the coherent backscatter opposition effect terms are utilized. The solution that minimizes χ^2 for the model with the coherent backscatter opposition effect is smaller than that for the model without this effect. The Shevchenko function parameter a for Vesta identifies it as being on the high-albedo side, but near the peak (Fig 7). This implies that the opposition effect consists not only of the shadow-hiding effect, but also the coherent backscattering effect.

Fig. 5(b) highlights that the contribution of the coherent backscattering enhancement of Vesta appears at ca. 1.0°. Mishchenko, Rosenbush, & Kiselev (2006) showed that the phase dependencies of the degree of linear polarization have a narrow local minimum of negative polarization centered at a phase angle that is approximately equal to a half-width of the corresponding coherent backscattering opposition effect. Velichko et al. (2008) demonstrated that a phase dependence in polarization exists for Vesta within a range of phase angles from 0.6° to 24.7°, and that a narrow local minimum of negative polarization does not appear at greater than 1.5°. The aforementioned features indicate that coherent backscattering enhancement contributes to scattering of Vesta at less than 1.0°.

The width of the coherent backscattering opposition effect peak h_{C_λ} from the Hapke model, which is interpreted in terms of the wavelength and transport mean free path in the medium (Hapke 2002), is given by:

$$h_{C_\lambda} = \frac{\lambda}{4\pi\Lambda_\lambda}, \tag{17}$$

where λ is the wavelength and Λ is the transport mean free path in the medium.

Table 6 lists h_{C_λ}, λ, Λ_λ, and mean regolith particle sizes for asteroids, the Moon, and Jovian and Saturnian satellites. Λ_λ in the regolith of Vesta, the Moon, and asteroid 2867 Steins is approximately one and a half orders of magnitudes smaller than the mean particle size. This can be explained, as the coherent backscattering opposition appears to be linked to the most tegmental particles. Theoretical models of the coherent backscattering opposition effect predict that h_{C_λ} should be proportional to the wavelength, but no wavelength dependence on width has been experimentally shown for the Moon (Hapke et al. 2012). This fact is supported by weak dependence between wavelength and h_{C_λ} for Enceladus and Phoebe. The value of h_{C_λ} for Vesta seems to be affected by the wavelength of the observations. Since h_{C_λ} in this study is defined by only three points, it is really hard to say whether it is wavelength-dependent.

Hapke (2002) did not identify any relationship between the strength B_{C0} of the coherent backscattering term and any other parameters, but Hillier, Buratti, & Hill et al. (1999), who used the Hapke model with minor changes to the coherent backscatter term (Helfenstein et al. 1997), suggested that B_{C0} is related to the fraction of light that is multiply scattered within a single particle and, hence, related to particle structure. However, the relevance of B_{C0} and other parameters has not been investigated using observational data. Table 5 shows that

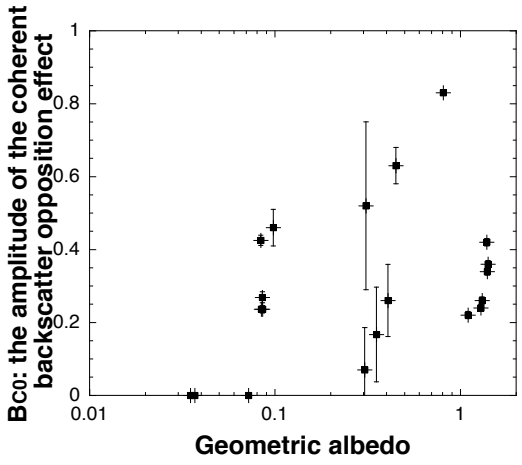

Fig. 9. Comparison of the strength B_{C0} of the coherent backscattering term for solar system objects. B_{C0} values for the asteroids 588 Achilles, 884 Priamus, and 1143 Odysseus are taken as being zero, due to their lack of non-linear opposition brightening. The values for Jovian Trojan asteroids, Steins, Moon, and Galilean satellites were taken from Usui et al. (2011), Lamy et al. (2008), Lane & Irvine (1973), and Buratti (1995), respectively.

B_{C0} for Vesta is enhanced, as the reflectance of Vesta is high relative to the wavelength. The spectral ratio of less than 1.0° generally increases with longer wavelength (Kaydash et al. 2013). Moreover, the intensity of the lunar spectra in Kaydash et al. (2013) appears to redden. Thus, B_{C0} for the Moon is also enhanced at increased reflectance. Figure 9 implies that B_{C0_λ} for solar system objects tends to increase when surface reflectivity increases. These facts suggest that a relationship exists between B_{C0_λ} and reflectance. Li et al. (2013) showed that about 20%–30% of scattered light on the surface of Vesta is multiply scattered. Shevchenko et al. (2012) proposed that an absence of opposition effects for low-albedo objects can be interpreted to result from their very dark surfaces in which only single-light scattering is important. Therefore, multiple-scattering on an optically active scale may contribute to the coherent backscattering term on the surface.

6. Summary

B, $R_{\rm C}$, and z' band photometric observations of Vesta were carried out, including measurements at very low phase angles. The magnitudes at a phase angle of 0° in each band are $M_B(1, 1, 0) = 3.83 \pm 0.01$, $M_{R_{\rm C}}(1, 1, 0) = 2.67 \pm 0.01$, and $M_{z'}(1, 1, 0) = 3.03 \pm 0.01$ mag. The absolute magnitude obtained using the IAU H–G function is ∼0.1 mag darker than that at the phase angle of 0° determined from the Shevchenko function and Hapke models with the coherent backscattering effect term. The Hapke model analysis of the obtained data resulted in a geometric albedo of 0.35 in the B band, 0.41 in the $R_{\rm C}$ band, and 0.31 in the z' bands. The bulk density of the optically active regolith on Vesta was estimated based on the Hapke

model at 0.9–2.0 $\times$ 10^3 kg m^{-3}. The coherent backscattering effect contributes to the opposition effect on the surface of Vesta, at least at values below 1.0°. The amplitude of the coherent backscatter opposition effect for solar system objects, apart from extreme high-albedo objects, increases as geometric albedo increases. This supports the multiple-scattering interpretation of the coherent backscattering term on Vesta.

We thank the staff members of the Maidanak Astronomical Observatory for their support during photometric observations. We are grateful to Jian-Yang Li for sharing valuable details of Dawn spacecraft observations of Vesta. We thank an anonymous reviewer for their careful and constructive reviews, which helped improve the manuscript significantly. This study was supported by the National Research Foundation of Korea (NRF) grant funded by the Korea Government (MEST) (No. 2012R1A4A1028713), Optical & Near-Infrared Astronomy Inter-University Cooperation Program, the MEXT of Japan, and the Space Plasma Laboratory, ISAS, JAXA, as a collaborative research program.

References

Allen, C. W. 1976, Astrophysical Quantities (London: The Athlone Press)

Allen, D. A. 1970, Nature, 227, 158

Aspin, J. 1825, A Familiar Treatise on Astronomy: Explaining the General Phenomena of Celestial Bodies (London: Samuel Leigh)

Barabashev, N. P. 1922, Astron. Nachr., 217, 445

Belskaya, I. N., & Shevchenko, V. G. 2000, Icarus, 147, 94

Belskaya, I. N., et al. 2002, in Proceedings of Asteroids, Comets, Meteors - ACM 2002, ed. B. Warmbein (Netherlands: ESA Publications Division), 489

Belskaya, I. N., et al. 2003, Icarus, 166, 276

Bobrovnikoff, N. T. 1929, Lick Obs. bull., 407, 18

Boggess, A., et al. 1978, Nature, 275, 372

Bowell, E., Hapke, B., Domingue, D., Lumme, K., Peltoniemi, J., & Harris, A. W. 1989, in Asteroids Ⅱ, ed. R. P. Binzel, T. Gehrels, & M. Shapely (Tucson: University of Arizona Press), 524

Britt, D. T., & Consolmagno, G. J. 2002, Meteorit. Planet. Sci., 38, 1161

Buratti, B. J. 1995, J. Geophys. Res., 100, 19061

Bus, S. J., & Binzel, R. P. 2002, Icarus, 158, 106

Butterworth, P. S. , Meadows, A. J., Hunt, G. E., Moore, V., & Willis, D. M. 1980, Nature, 287, 701

Carrier, W. D., Ⅲ 1970, Moon, 6, 250

Degewij, J., Tedesco, E. F., & Zellner, B. 1979, Icarus, 40, 364

De Sanctis M. C., et al. 2013, Meteorit. Planet. Sci., 48, 2166

Dlugach, Zh. M., & Mishchenko, M. I. 2013, Astronomicheskii Vestnik, 47, 494

Domingue, D. L. , Robinson, M., Carcich, B., Joseph, P., Thomas, P., & Clark, B. E. 2002, Icarus, 155, 205

Dotto E., et al. 2000, A&A, 358, 1133

Drummond, J. D. , Eckart, A., & Hege, E. K. 1988, Icarus, 73, 1
Filippenko, A. V. 1982, PASP, 323, 606
Franklin, F. A., & Cook, A. F. 1974, Icarus, 23, 355
Fornasier, S., Mottola, S., Barucci, M. A., Sierks, H., & Hviid, A. 2011, A&A, 53, L9
Fulvio, D., Blanco, C., Cigna, M., & Gandolfi, D. 2008, Mem. S. A. It. Siuppl., 12, 12
Gehrels, T. 1956, ApJ, 123, 331
Gehrels, T. 1967, AJ, 72, 929
Gehrels, T., & Taylor, R. C. 1977, AJ, 82, 229
Glassmeier, K.-H., Boehnhardt, H., Koschny, D., Kührt, E., & Ingo, H. 2007, Space Sci. Rev., 128, 1
Gundlach, B., & Blum, J. 2013, Icarus, 223, 479
Hapke, B. 1981, J. Geophys. Res., 86, 3039
Hapke, B. 1984, Icarus, 59, 41
Hapke, B. 1986, Icarus, 67, 264
Hapke, B. 2002, Icarus, 157, 523
Hapke, B. 2008, Icarus, 195, 918
Hapke, B., Denevi, B., Sato, H., Braden, S., & Robinson, M. 2012, J. Geophys. Res., 117, E00H15
Harrington, M. W. 1883, Amer. J. Sci., 26, 464
Harris, A. W., et al. 1989, Icarus, 81, 365
Hasegawa, S., Abe, M., Tokimasa, N., & Ozaki, S. 2006, in Proc. 39th ISAS Lunar Planet. Symp., ed. M. Kato & S. Tanaka (Sagamihara: Institute of Space and Astronautical Science), 186
Hasegawa, S., Miyasaka, S., Tokimasa, N., Sogame, A., Ibrahimov, M. A., Yoshida, F., Abe, M., & Kuroda, D. 2009, Lunar Planet. Sci., 40, 1530
Hasegawa, S., Murakawa, K., Ishiguro, M., Nonaka, H., Takato, N., Davis, C. J., Ueno, M., & Hiroi, T. 2003, Geophys. Res. Lett., 30, 2123
Helfenstein, P., & Shepard, M. K. 2011, Icarus, 215, 83
Helfenstein, P., & Veverka, J. 1987, Icarus, 72, 342
Helfenstein, P., & Veverka, J. 1989, in Asteroids Ⅱ, ed. R. P. Binzel, T. Gehrels, & M. Shapely (Tucson: University of Arizona Press), 557
Helfenstein, P., Veverka, J., & Hillier, J. 1997, Icarus, 128, 2
Henyey, L. G., & Greenstein, J. L. 1941, ApJ, 93, 70
Heras, A. M., Morris, P. W., Vandenbussche, B., & Müller, T. G. 2000, in Thermal Emission Spectroscopy and Analysis of Dust, Disks, and Regoliths, ed. M. L. Sitko, A. L. Sprague, & D. K. Lynch, ASP Conf. Ser., 196, 205
Hertz, H. G. 1968, Science, 160, 299
Hicks, M. D., Fink, U., & Grundy, W. M. 1998, Icarus, 133, 69
Hicks, M. D., et al. 2014, Icarus, 235, 60
Hillier, J. K., Buratti, B. J., & Hill, K. 1999, Icarus, 141, 205
Hiroi, T., Pieters, C. M., & Takeda, H. 1994, Meteoritics, 29, 394
Houston, W. N., Mitchell, J. K., & Carrier, W. D., Ⅲ 1974, Proc. fifth Lunar Planet. Sci. conf. Suppl. 5, Geochim. Cosmochim. Acta, 3, 2361
Ishigaki, T., et al. 2004, PASJ, 56, 723

Ivezić, Ž., et al. 2001, AJ, 122, 2749
Johnston, K. J., Lamphear, E. J., Webster, W. J., Lowman, P. D., Seidelmann, P. K., Kaplan, G. H., Wade, C. M., & Hobbs, R. W 1989, AJ, 98, 335
Jaumann, R., Nathues A., Mottola, S., & Hoffmann, H. 1996, in Workshop on Evolution of Igneous Asteroids: Focus on Vesta and the HED Meterorites, ed. D. W. Mittlefehldt & J. J. Papike (Houston: Lunar and Planetary Institute), 13
Jaumann, R., et al. 2012, Science, 336, 687
Kaydash, V., Pieters, C., Shkuratov, Y., & Korokhin, V. 2013, J. Geophys. Res., 118, 1221
Keller, H. U. et al. 2007, Space Sci. Rev., 128, 433
Kessler, M. F. et al. 1996, A&A, 315, L27
Lagerkvist, C.-I., & Magnusson, P. 1990, A&AS, 86, 119
Lagerkvist, C.-I., & Williams, I. P. 1987, A&AS, 68, 295
Lagerkvist, C.-I., Magnusson, P., Williams, I. P., Buontempo, M. E., Argyle, R. W., & Morrison, L. V. 1992, A&AS, 94, 73
Lagerkvist, C.-I., Magnusson, P., Williams, I. P., Buontempo, M. E., Gibbs, P., & Morrison, L. V. 1988, A&AS, 73, 395
Lagerkvist, C.-I., Magnusson, P., Williams, I. P., Buontempo, M. E., Gibbs, P., & Morrison, L. V. 1989, A&AS, 78, 519
Lamy, P. L., et al. 2008, A&A, 4897, 1187
Lane, A. P., & Irvine, W. M. 1973, AJ, 78, 267
Larson, H. P., & Fink, U. 1975, Icarus, 26, 420
Li, J.-Y., et al. 2010, Icarus, 208, 238
Li, J.-Y., et al. 2011, Icarus, 216, 640
Li, J.-Y., et al. 2013, Icarus, 226, 1252
McCord, T., Adams, J., & Johnson, T. V. 1970, Science, 168, 1445
McKay, D. S., Swindle, T. D., & Greenberg, R. 1989, in Asteroids Ⅱ, ed. R. P. Binzel, T. Gehrels, & M. Shapely (Tucson: University of Arizona Press), 617
Miller, C., Verbiscer, A. J., Chanover, N. J., Holtzman, J. A., & Helfenstein, P. 2011, Icarus, 221, 819
Mishchenko, M. I., Rosenbush, V. K., & Kiselev, N. H. 2006, Appl. Opt., 45, 4459
Mitchell, D. L., et al. 1996, Icarus, 124, 113
Muinonen, K., Piironen, J., Shkuratov, Yu.G., Ovcharenko, A., & Clark, B. E. 2002, in Asteroids Ⅲ, ed. W. F. Bottke, A. Cellino, P. Paolicchi, & R. P. Binzel (Tucson: University of Arizona Press), 123
Müller, T. G., & Lagerros, J. S. V. 1998, A&A, 338, 340
Neugebauer G. et al. 1984, ApJ, 278, L1
Nonaka, H., Ishiguro, M., Abe, M., Sogame, A., Nishiura, S., & Hasegawa, S. 2003, in Proc. 36th ISAS Lunar Planet. Symp., ed. H. Mizutani & M. Kato (Sagamihara: Institute of Space and Astronautical Science), 181
Ohtani, T., et al. 1998, Proc. SPIE, 3355, 750
Oja, T. 1996, Baltic Astron., 5, 103

O'Leary, B. T. 1967, AJ, 149, 147
Piironen, J., Magnusson, P., Lagerkvist, C.-I., Williams, I. P., Buontempo, M. E., & Morrison, L. V. 1997, A&AS, 121, 489
Ramírez, I., et al. 2012, ApJ, 752, 5
Reddy, V., et al. 2012, Icarus, 217, 153
Redman, R. O., Feldman, P. A., Matthews, H. E., Halliday, I., & Creutzberg, F. 1992, AJ, 104, 405
Reynoldson, G., Thacker, P., Ericson, A., & Oja, T. 1993, Minor Planet Bul., 20, 11
Rock, J. W., & Hollis, A. J. 1990, J. Br. Astron. Assoc., 100, 1
Rodgers, C. T., Canterna, R., Smith, J. A., Pierce, M. J., & Tucker, D. L. 2006, AJ, 132, 989
Russell, C. T., et al. 2012, Science, 336, 684
Scaltriti, F., & Zappalà, V. 1980, aap, 83, 249
Schröder, S. E., Maue, T., Gutiérrez Marqués, T., Mottola, S., Aye, K. M., Sierks, H., Keller, H. U., & Nathues, A. 2013, Icarus, 226, 1304
Seeliger, H. 1895, Abh. Bayer. Acad. Wiss. Math. Naturwiss. Kl., 18, 1
Shepard, M. K., & Helfenstein, P. 2007, J. Geophys. Res., 112, E03001
Shepard, M. K., & Helfenstein, P. 2011, Icarus, 215, 526
Shevchenko, V. G. 1996, Lunar Planet. Sci., 27, 1193
Shevchenko, V. G., Belskaya, I. N., Chiorny, V. G., Piironen, J., Erikson, A., Neukum, G., & Mohamed, R. 1997, Planet. Space Sci., 45, 1615
Shevchenko, V. G., Belskaya, I. N., Krugly, Yu. N., Chiorny, V. G., & Gaftonyuk, N. M. 2002, Icarus, 155, 365
Shevchenko, V. G., Chiorny, V. G., Gaftonyuk, N. M., Krugly, Yu. N., Belskaya, I. N., Tereschenko, I. A., & Velichko, F. P. 2008, Icarus, 196, 601
Shevchenko, V. G., et al. 2012, Icarus, 217, 202
Stephenson, C. B. 1951, AJ, 114, 500
Smith, J. A., et al. 2002, AJ, 123, 2121
Sogame, A., Saito, J., Hasegawa, S., & Ishiguro, M. 2005, Journal of the Remote Sensing Society of Japan, 25, 372
Spjuth, S., Jorda, L., Lamy, P. L., Keller, H. U., & Li, J.-Y. 2012, Icarus, 221, 1101
Taylor, R. C. 1973, AJ, 78, 1131
Thomas, P. C., Binzel. R. P., Gaffey, M. J., Storrs, A. D., Wells, E. N., & Zellner, B. H. 1997, Science 277, 1492
Thompson, D. T., & Lockwood, G. W. 1992, J. Geophys. Res., 97, 14761
Usui, F., Hasegawa, S., Ishiguro, M., Müller, T. G., & Ootsubo, T. 2014, PASJ, in press
Usui, F., Kasuga, T., Hasegawa, S., Ishiguro, M., Kuroda, D., Müller, T. G., Ootsubo, T., & Matsuhara, H. 2013, ApJ, 732, 56
Usui, F., et al. 2011, PASJ, 63, 1117
Worden, S. P., Stein, M. K., Schmidt, G. D., & Angel, J. R. P. 1977, Icarus, 32, 450
Velichko, F. P., Rosenbush, V. K., Krugly, Yu. N., Kiselev, N. N. Velichko, S. F., Antonyuk, K. A., & Shevchenko, V. G. 2008, in Proc. the Solar System Bodies: From Optics To Geology, ed. Yu. G. Shkuratov et al. (Kharkiv: V.N. Karazin National University), 123

Verbiscer, A. J., French, R. G., & McGhee, C. A. 2005, Icarus, 173, 66
Zellner, B., Tholen, D. J., & Tedesco, E. F. 1985, Icarus, 61, 355

Table 1. Nightly details of the photometric observations.*

Date	Time (UT)	$R_{\rm h}$	Δ	α	Telescope	Filter
[year.month.day]	[hour.minute.second]	[AU]	[AU]	[°]		band
2005.Dec.01	12:32:31 – 18:34:31	2.552	1.741	15.3	0.064 m – Sagamihara	$BR_{\rm C}z'$
2005.Dec.08	12:37:18 – 19:09:15	2.549	1.680	12.8 – 12.9	0.064 m – Sagamihara	$BR_{\rm C}z'$
2005.Dec.09	12:48:40 – 20:02:04	2.549	1.672	12.4 – 12.5	0.064 m – Sagamihara	$BR_{\rm C}z'$
2005.Dec.22	11:47:41 – 19:20:44	2.543	1.590	6.8 – 7.0	0.064 m – Sagamihara	$BR_{\rm C}z'$
2005.Dec.24	11:17:38 – 18:44:57	2.542	1.581	6.0 – 6.1	0.064 m – Sagamihara	$BR_{\rm C}z'$
2005.Dec.28	11:30:15 – 16:04:49	2.540	1.567	4.1 – 4.2	0.064 m – Sagamihara	$BR_{\rm C}z'$
2005.Dec.30	11:04:36 – 17:53:25	2.539	1.562	3.1 – 3.2	0.064 m – Sagamihara	$BR_{\rm C}z'$
	12:25:34 – 19:01:15	2.539	1.562	3.1 – 3.2	0.36 m – Miyasaka	$BR_{\rm C}z'$
2005.Dec.31	13:03:20 – 18:40:14	2.539	1.559	2.6 – 2.7	0.36 m – Miyasaka	$BR_{\rm C}z'$
2006.Jan.02	12:46:02 – 19:49:22	2.538	1.556	1.6 – 1.7	0.36 m – Miyasaka	$BR_{\rm C}z'$
2006.Jan.03	10:52:58 – 19:10:20	2.537	1.555	1.1 – 1.3	0.064 m – Sagamihara	$BR_{\rm C}z'$
	11:34:44 – 18:41:44	2.537	1.555	1.1 – 1.2	0.36 m – Miyasaka	$BR_{\rm C}z'$
	12:49:43 – 13:30:33	2.537	1.555	1.2	0.076 m – Nishiharima	$BR_{\rm C}z'$
2006.Jan.05	10:09:27 – 17:12:14	2.536	1.553	0.2 – 0.3	0.064 m – Sagamihara	$BR_{\rm C}z'$
	10:18:27 – 20:15:35	2.536	1.553	0.1 – 0.3	0.36 m – Miyasaka	$BR_{\rm C}z'$
	14:25:09 – 16:05:04	2.536	1.553	0.2	0.076 m – Nishiharima	$BR_{\rm C}z'$
	22:31:43 – 23:28:47	2.536	1.553	0.1	0.60 m – Maidanak	$BR_{\rm C}$
2006.Jan.06	15:02:09 – 19:32:53	2.535	1.552	0.4	0.36 m – Miyasaka	$BR_{\rm C}z'$
	16:33:20 – 16:59:32	2.535	1.552	0.4	0.076 m – Nishiharima	$BR_{\rm C}z'$
2006.Jan.07	10:26:21 – 17:50:14	2.535	1.552	0.8 – 0.9	0.064 m – Sagamihara	$BR_{\rm C}z'$
	10:42:44 – 19:10:30	2.535	1.552	0.8 – 0.9	0.36 m – Miyasaka	$BR_{\rm C}z'$
2006.Jan.08	10:36:44 – 14:33:54	2.535	1.552	1.2 – 1.3	0.064 m – Sagamihara	$BR_{\rm C}z'$
	10:31:09 – 16:55:31	2.535	1.552	1.2 – 1.4	0.36 m – Miyasaka	$BR_{\rm C}z'$
2006.Jan.25	10:20:59 – 17:59:58	2.525	1.598	9.4 – 9.5	0.064 m – Sagamihara	$BR_{\rm C}z'$
2006.Jan.27	10:43:40 – 17:37:28	2.524	1.608	10.2 – 10.4	0.064 m – Sagamihara	$BR_{\rm C}z'$
	12:59:10 – 13:48:06	2.524	1.608	10.3	0.36 m – Miyasaka	$BR_{\rm C}z'$
2006.Jan.28	09:01:31 – 15:18:34	2.523	1.613	10.6 – 10.8	0.36 m – Miyasaka	$BR_{\rm C}z'$
2006.Feb.04	09:22:49 – 15:21:43	2.519	1.659	13.5 – 13.6	0.36 m – Miyasaka	$BR_{\rm C}z'$
2006.Feb.11	09:46:00 – 15:43:07	2.515	1.715	16.0	0.36 m – Miyasaka	$BR_{\rm C}z'$
2006.Feb.17	10:57:56 – 16:31:04	2.511	1.770	17.8 – 17.9	0.36 m – Miyasaka	$BR_{\rm C}z'$
2006.Feb.18	12:50:01 – 16:05:04	2.510	1.779	18.1	0.076 m – Nishiharima	$BR_{\rm C}z'$
2006.Feb.23	10:57:25 – 14:49:22	2.506	1.829	19.4	0.076 m – Nishiharima	$BR_{\rm C}z'$
2006.Mar.03	09:29:08 – 11:33:53	2.501	1.915	21.0 – 21.1	0.36 m – Miyasaka	$BR_{\rm C}z'$
2006.Mar.04	09:36:50 – 11:44:23	2.501	1.927	21.2	0.36 m – Miyasaka	$BR_{\rm C}z'$

Table 1. (Continued.)

Date	Time (UT)	$R_{\rm h}$	Δ	α	Telescope	Band
2006.Mar.14	09:34:59 – 15:09:59	2.493	2.044	22.6 – 22.7	0.064 m – Sagamihara	$BR_{\rm C}z'$
2006.Mar.15	09:36:09 – 12:17:59	2.493	2.055	22.8	0.064 m – Sagamihara	$BR_{\rm C}z'$
2006.Mar.20	09:42:59 – 12:12:18	2.489	2.115	23.2	0.064 m – Sagamihara	$BR_{\rm C}z'$
	11:05:51 – 13:42:03	2.489	2.116	23.2	0.076 m – Nishiharima	$BR_{\rm C}z'$
2006.Mar.29	10:54:30 – 13:53:58	2.482	2.225	23.7	0.064 m – Sagamihara	$BR_{\rm C}z'$
2006.Mar.31	09:43:42 – 13:49:44	2.480	2.250	23.7 – 23.8	0.064 m – Sagamihara	$BR_{\rm C}z'$
2006.Apr.03	10:47:08 – 13:33:19	2.478	2.287	23.8	0.076 m – Nishiharima	$BR_{\rm C}z'$

* The heliocentric distance ($R_{\rm h}$), geocentric distance (Δ), and phase angle (α) for observing asteroids were obtained by the JPL HORIZON ephemeris generator system of NASA.[1]

Table 2. Nightly details of spectroscopic observations.

Date	Time (UT)	$R_{\rm h}$	Δ	α	Telescope	Integration	Airmass
[year.month.day]	[hour.minute.second]	[AU]	[AU]	[°]		time [sec]	
2006.Feb.27	13:43:09 – 14:01:42	2.504	1.873	20.3	2.0 m – Nishiharima	4 × 100	1.24
2006.Mar.02	13:40:32 – 13:49:24	2.501	1.905	20.9	2.0 m – Nishiharima	4 × 100	1.25
2006.Mar.02	14:22:55 – 14:32:12	2.501	1.906	20.9	2.0 m – Nishiharima	4 × 100	1.43
2006.Mar.02	14:51:53 – 15:00:30	2.501	1.906	20.9	2.0 m – Nishiharima	4 × 100	1.61
2006.Mar.02	15:20:29 – 15:32:05	2.501	1.906	20.9	2.0 m – Nishiharima	4 × 100	1.87
2014.Jan.28	19:37:39 – 19:39:03	2.287	1.862	24.9	1.88 m – Okayama	2 × 10	1.27
2014.Jan.28	19:46:06 – 19:47:45	2.287	1.862	24.9	1.88 m – Okayama	2 × 10	1.26
2014.Jan.28	19:57:41 – 19:59:50	2.287	1.862	24.9	1.88 m – Okayama	2 × 10	1.25

Table 3. Comparison of IAU H–G phase functions for Vesta.

H_λ [mag]	G_λ	Filter band ([μm])*	α [°]	References
3.96	**0.30**	***B***	**0.1 – 52.3**	**This study**
⟨0.01⟩	⟨0.02⟩			Fitting error‡
——	0.32	F8 (0.44)	3.8 – 25.7	Reddy et al. (2012)
2.82	**0.29**	$\boldsymbol{R_C}$	**0.1 – 81.3**	**This study**
⟨0.01⟩	⟨0.01⟩			Fitting error‡
2.81	0.27	R_C	0.1 – 23.8	This study
2.85	0.31	R_C	1.0 – 23.8	This study
2.81	0.27	R_C	7.0 – 23.8	This study
2.82	0.28	R_C	0.1 – 43.1	This study
2.82	0.28	R_C	0.1 – 52.3	This study
2.87	0.39	R_C	0.1 – 108.6	This study
2.80	0.27	R_C	0.1† – 52.3	Fornasier et al. (2011)
——	0.29	F7 (0.65)	3.8 – 25.7	Reddy et al. (2012)
3.08	**0.25**	***z′***	**0.1 – 52.3**	**This study**
⟨0.01⟩	⟨0.01⟩			Fitting error‡
——	0.36	F4 (0.92)	3.8 – 25.7	Reddy et al. (2012)
3.16	0.34	V	——	Minor Planet Circ. 11095 (1986)
3.38	0.47	V	5.9 – 25.5	Lagerkvist & Williams (1987)
3.28	0.41	V	4.9 – 23.4	Lagerkvist et al. (1988)
3.25	0.35	V	1.4 – 22.6	Lagerkvist et al. (1989)
3.40	0.33	V	1.7 – 23.7	Lagerkvist & Magnusson (1990)
3.20	0.32	V	——	Minor Planet Circ. 17256 (1990)
3.32	0.42	V	1.3 – 28.1	Rock & Hollis (1990)
——	0.35	V	1.2 – 26.1	Lagerkvist & Magnusson (1990)
3.19	0.32	V	4.9 – 25.3	Piironen et al. (1997)
3.14	0.32	V	0.4 – 24.8	Velichko et al. (2008)
——	0.23	F2 (0.56)	3.8 – 25.7	Reddy et al. (2012)
3.2	0.28	V	1.7 – 108.6	Li et al. (2013)

*Values in parentheses are the effective wavelength of the Framing Camera onboard the Dawn spacecraft.
†Data in Fornasier et al. (2011) include preliminary data from this study (Hasegawa et al. 2009).
‡Fitting errors appear within brackets below each parameter value.

Table 4. Comparison of the Shevchenko function for Vesta.

$M_\lambda(1, 1, 0)$ [mag]	a_λ	b_λ [mag/°]	C_λ [mag]	Filter band (eff. λ [μm])	α [°]	References
3.85	**0.427**	**0.0259**	**4.271**	***B***	**0.1 − 52.3**	**This study**
⟨0.01⟩	⟨0.037⟩	⟨0.0008⟩	⟨0.018⟩			Fitting error*
2.71	**0.416**	**0.0269**	**3.127**	$\boldsymbol{R_C}$	**0.1 − 81.3**	**This study**
⟨0.01⟩	⟨0.037⟩	⟨0.0003⟩	⟨0.012⟩			Fitting error*
2.98	**0.416**	**0.0278**	**3.400**	***z′***	**0.1 − 52.3**	**This study**
⟨0.01⟩	⟨0.031⟩	⟨0.0008⟩	⟨0.014⟩			Fitting error*

*Fitting errors appear within brackets below each parameter value.

Table 5. Comparison of the Hapke model for Vesta.

$M_\lambda(1, 1, 0)$ [mag]	w_λ	g_λ	$\bar{\theta_\lambda}$* [°]	B_{S0_λ}	h_{S_λ} [rad]	B_{C0_λ}	h_{C_λ} [rad]	A_{p_λ}	q_λ	A_{B_λ}	Band	References
3.83	**0.417**	**-0.282**	**(18.4)**	**1.19**	**0.052**	**0.167**	**0.0034**	**0.353**	**0.415**	**0.146**	***B***	**This study**
⟨0.01⟩	⟨0.014⟩	⟨0.035⟩	—	⟨0.20⟩	⟨0.023⟩	⟨0.130⟩	⟨0.0060⟩	⟨0.004⟩	⟨0.004⟩	⟨0.002⟩		Fitting error†
3.93	0.421	-0.310	(18.4)	1.10	0.032	—	—	0.321	0.450	0.145	B	This study
⟨0.01⟩	⟨0.012⟩	⟨0.020⟩	—	⟨0.09⟩	⟨0.006⟩	—	—	⟨0.003⟩	⟨0.005⟩	⟨0.002⟩		Fitting error†
—	0.393	-0.208	18.4	1.87	0.100	—	—	0.287	0.526	0.151	F8‡	Li et al. (2013)§
2.67	**0.454**	**-0.177**	**(17.8)**	**2.05**	**0.086**	**0.260**	**0.0057**	**0.407**	**0.420**	**0.171**	$\boldsymbol{R_C}$	**This study**
⟨0.01⟩	⟨0.020⟩	⟨0.029⟩	—	⟨0.33⟩	⟨0.028⟩	⟨0.099⟩	⟨0.0061⟩	⟨0.004⟩	⟨0.004⟩	⟨0.002⟩		Fitting error†
2.88	0.464	-0.189	(17.8)	2.09	0.067	—	—	0.335	0.507	0.170	R_C	This study
⟨0.01⟩	⟨0.011⟩	⟨0.019⟩	—	⟨0.23⟩	⟨0.011⟩	—	—	⟨0.003⟩	⟨0.005⟩	⟨0.002⟩		Fitting error†
—	0.556	-0.243	17.8	1.83	0.047	—	—	0.462	0.474	0.219	F7‡	Li et al. (2013)§
3.03	**0.373**	**-0.303**	**(18.8)**	**1.17**	**0.040**	**0.070**	**0.0091**	**0.305**	**0.415**	**0.127**	***z′***	**This study**
⟨0.01⟩	⟨0.011⟩	⟨0.027⟩	—	⟨0.17⟩	⟨0.026⟩	⟨0.116⟩	⟨0.0332⟩	⟨0.003⟩	⟨0.004⟩	⟨0.001⟩		Fitting error†
3.06	0.374	-0.314	(18.8)	1.18	0.031	—	—	0.298	0.419	0.125	z'	This study
⟨0.01⟩	⟨0.009⟩	⟨0.016⟩	—	⟨0.08⟩	⟨0.005⟩	—	—	⟨0.003⟩	⟨0.004⟩	⟨0.001⟩		Fitting error†
—	0.365	-0.225	18.8	1.59	0.097	—	—	0.256	0.531	0.136	F4‡	Li et al. (2013)§
—	0.40	-0.30	(20)	1.03	0.044	—	—	—	—	—	V	Helfenstein & Veverka (1989)
3.20	0.424	-0.150	(18.0)	2.60	0.120	—	—	0.329	0.538	0.177	V	Li et al. (2013)‖
—	0.554	-0.244	17.5	1.83	0.048	—	—	0.417	0.468	0.195	F2‡	Li et al. (2013)§
—	0.51	-0.26	31.5	1.0	0.098	—	—	0.34	0.44	0.15	V	Hicks et al. (2014)#

*Assumed values were kept constant in the data fitting.
†Fitting errors appear within brackets below each parameter value.
‡See the third column in Table 3.
§The values were obtained from disk-resolved data of Vesta from approach and survey using color filters.
‖The solutions were obtained from the disk-integrated phase function of Vesta using approach data taken through a clear filter.
#The values were obtained from photometric data using not only Vesta but also several V-type asteroids.

Table 6. Comparison of the transport mean free path in a medium.

Object		h_{C_λ}	λ	Λ_λ	regolith grain	References
		°	[μm]	[μm]	size* [μm]	
4 Vesta	0.20	B	10.6	108		This study
4 Vesta	0.33	R_C	8.9	108		This study
4 Vesta	0.89	z'	4.7	108		This study
Enceladus	0.645	0.34	2.4	—		Verbiscer et al. (2005)
Enceladus	0.17	0.55	14.6	—		Verbiscer et al. (2005)
Enceladus	0.28	0.87	14.1	—		Verbiscer et al. (2005)
Europa	0.08	0.47	26.7	—		Verbiscer et al. (2005)
Ganymede	0.22	0.47	9.8	—		Verbiscer et al. (2005)
2867 Steins	0.14	0.63	20.1	1260		Spjuth et al. (2012)
Moon	2.27	0.56	1.1	96		Verbiscer et al. (2005)
Phoebe	0.64	B	3.4	—		Miller et al. (2011)
Phoebe	0.81	R	3.6	—		Miller et al. (2011)
Phoebe	0.82	I	4.6	—		Miller et al. (2011)

* Data on regolith grain size were taken from Gundlach & Blum (2013).